Hybrid atomistic–continuum method for the simulation of dense fluid flows

Thomas Werder, Jens H. Walther, Petros Koumoutsakos *

Institute of Computational Science, ETH Zürich HRS H12, Hirschengraben 84, CH-8092 Zürich, Switzerland

Abstract

We present a hybrid atomistic–continuum method for multiscale simulations of dense fluids. In this method, the atomistic part is described using a molecular dynamics description, while the continuum flow is described by a finite volume discretization of the incompressible Navier–Stokes equations. The two descriptions are combined in a domain decomposition formulation using the Schwarz alternating method. A novel method has been proposed in order to impose non-periodic velocity boundary conditions from the continuum to the atomistic domain, based on an effective boundary potential, consistent body forces, a particle insertion algorithm and specular walls. The extraction of velocity boundary conditions for the continuum from the atomistic domain is formulated by taking into account the associated statistical errors. The advantages and drawbacks of the proposed Schwarz decomposition method as compared to related flux-based schemes are discussed. The efficiency and applicability of the method is demonstrated by considering hybrid and full molecular dynamics simulations of the flow of a Lennard–Jones fluid past a carbon nanotube.
© 2004 Elsevier Inc. All rights reserved.

Keywords: Multiscale simulation; Hybrid algorithms; Molecular dynamics; Nanofluidics

1. Introduction

The study of nanoscale fluid mechanics [1] is important for the understanding and development of nanoscale devices such as biosensors operating in aqueous environments. The behaviour of biosensors can be studied through a canonical problem involving carbon nanotubes (CNT) immersed in a liquid environment [2,3]. The simulation of liquid-nanotube interactions is often performed using atomistic methods such as

classical molecular dynamics (MD) and direct simulation Monte-Carlo (DSMC) techniques. A number of studies using atomistic methods has described fundamental fluid flow phenomena such as wetting [2], the moving contact line problem [4] and the validity of the no-slip boundary condition [3]. Nanoscale flows are often part of larger scale systems (as for example when nanofluidic channels are interfacing microfluidic domains) and in simulations we are confronted with an *inherently* multiscale problem. Despite the success of atomistic simulations, their limitations in accessible length and time scales are stringent and allow only for the analysis of elementary systems for rather short times. To illustrate these limitations, consider that the time step δt in a MD simulation is dictated by the fastest frequency one needs to resolve. For a simulation of pure water, $\delta t = 2$ fs when models with fixed O–H bonds and H–O–H angles are used; in other words, 500 million time steps are required for 1 μs of simulation time. With the optimistic assumption that the execution of a single time step takes 0.1 s, a total of some 19 months of CPU time is required.

As full atomistic simulations are prohibitively expensive, hybrid atomistic–continuum simulations are necessary in order to study large systems for reasonable times. In these hybrid multiscale simulations, we need to address two key issues, namely:

(A1) the identification of the atomistic and continuum domains,
(A2) and the appropriate coupling of length and time scales for the two descriptions.

Significant progress has been made in solving both of these problems in the case of rarefied gas flows [5,6]. However, for dense fluids the situation is more complex since the atomistic description involves *interacting* particles. Two classes of coupling schemes for dense fluids have been proposed: the first one is based on *direct flux exchange* [7–9] and the second one on the Schwarz alternating method [10,4]. In the context of direct flux exchange schemes, O'Connell and Thompson [7] have coupled an atomistic system with a continuum domain where the average momentum of the overlap particles is adjusted through constrained dynamics. Flekkøy et al. [8] have presented a hybrid model which is explicitly based on direct flux exchange between the particle region and the continuum region. Wagner et al. [11] pursued this approach and extended it to treat unsteady flows and energy exchange, cf. also the subsequent work by Delgado-Buscalioni and Coveney [9]. Finally, Nie et al. [12] proposed a modification of the scheme in [7] and applied it to an impulsively started Couette flow. Hadjiconstantinou and co-workers [10] pointed out that direct flux exchange schemes decouple length but not timescales.

Hybrid schemes have to exchange information at the interface between the different descriptions. The difficulty when passing information from the atomistic to the continuum part is that the atomistic quantities are inherently fluctuating. In this work, we present results where the coupling between the atomistic and continuum descriptions involves only mean flow fields. Mesoscopic descriptions may be necessary in order to seamlessly transfer information between fluctuations in the atomistic level and mean field quantities in the continuum level. We show – based on recent work by Hadjiconstantinou et al. [13] – that the flux exchange schemes [8,9] require an excessive amount of sampling of the atomistic region in order to obtain statistically meaningful estimates of the fluxes to the continuum. In order to circumvent these problems, we implement the alternating Schwarz method [10,4] which iteratively finds a consistent solution in the atomistic and continuum domain. The Schwarz method avoids the direct imposition of fluxes but ensures nevertheless flux continuity under the assumption that the transport coefficients of the two descriptions match in the overlap domain. In this work, in order to simulate dense fluid flows, we extend the technique proposed in [4] to handle non-periodic systems thus broadening considerably the range of application of the Schwarz alternating scheme.

The outline of the paper is as follows: In Section 2, we review the alternating Schwarz method in the context of hybrid simulations of dense fluid flows. The imposition of boundary conditions from the continuum domain on the atomistic domain is discussed in Section 3. The finite volume discretization of the continuum domain and the extraction of boundary conditions from the atomistic for the continuum are treated

in Section 4. The proposed boundary model is validated in Section 5 and the overall method is applied to the flow of liquid argon around a carbon nanotube. The paper concludes by summarizing open issues and outlining future work.

2. Atomistic–continuum flows: the alternating Schwarz method

We consider hybrid atomistic–continuum simulations of dense fluid flows such as a liquid flow past a carbon nanotube. We implement a domain decomposition algorithm based on the alternating Schwarz method [14]. In this method, the flow domain Ω is decomposed into two overlapping regions: an atomistic region described by molecular dynamics and a continuum region described by a finite volume discretization of the incompressible Navier–Stokes equations. The fundamental assumption is that the atomistic and the continuum descriptions are valid and match in the overlapping domain.

In Fig. 1, we give an example of a hybrid domain used in the present work. The atomistic and the continuum domains are denoted as Ω_A and Ω_C, respectively. The boundary of the continuum domain is composed of an outer boundary $\partial\Omega_C$ and an inner boundary Γ_C that lies within the atomistic domain while the atomistic domain is bounded by an outer boundary Γ_A that lies within Ω_C. In each iteration n, the continuum velocity field u_C^n is computed in Ω_C with a given external boundary condition on $\partial\Omega_C$ and an internal boundary condition on Γ_C^n. The restriction of u_C^n to Γ_A^n is then the boundary condition for the atomistic problem in Ω_A whose solution u_A^n yields in turn the next continuum boundary condition Γ_C^{n+1}. The extraction of boundary conditions from the atomistic domain and the proper enforcement of boundary conditions on the atomistic domain represent major difficulties, as discussed in the following section.

The convergence of the hybrid velocity field toward an MD reference solution u_{MD} is measured by

$$e_{MD}^n = \frac{1}{N_\Omega} \sum_{k \in \Omega} \frac{|u_k^n - u_{k,MD}|}{u_\infty}, \tag{1}$$

where N_Ω is the number of cells in Ω, n is the iteration, and u_∞ is the freestream velocity. The cumulative average velocity u_k^n for cells $k \in \Omega_A$ is [15]

$$u_k^n = \frac{\sum_{j=1}^M \sum_{i \in k}^{N_k(t_j)} v_i(t_j)}{\sum_{j=1}^M N_k(t_j)}, \tag{2}$$

where M denotes the number of atomistic samples in iteration n, $N_k(t_j)$ is the number of particles in cell k at time t_j, and $v_i(t_j)$ is the velocity of particle i at time t_j. Furthermore, the rate of change of the velocity field is defined as
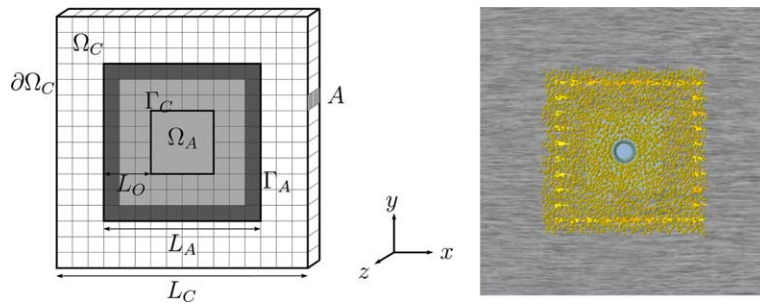

Fig. 1. Schematic of a hybrid atomistic/continuum computational domain. L_O denotes the size of the overlap domain between the atomistic domain Ω_A (entire shaded area) with boundary Γ_A (dark shaded area) and the continuum domain Ω_C with outer boundary $\partial\Omega_C$ and inner boundary Γ_C. The fine grid corresponds to the finite volume mesh and A is the area of a cell face. The right picture is a close-up of a hybrid computational domain to study the flow of liquid argon around a carbon nanotube as used in the present work.

$$d^n = \frac{1}{N_\Omega} \sum_{k \in \Omega} \frac{|\boldsymbol{u}_k^n - \boldsymbol{u}_k^{n-1}|}{u_\infty}. \tag{3}$$

3. Atomistic region: molecular dynamics of non-periodic systems

The atomistic region describes parts of the flow field, where the continuum assumptions fail and an atomistic representation is necessary in order to capture the physical properties of the system. In this work, the atomistic region is modeled using classical molecular dynamics (MD) simulations [16]. The positions $\boldsymbol{r}_i = (x_i, y_i, z_i)$ and velocities $\boldsymbol{v}_i = (v_{x,i}, v_{y,i}, v_{z,i})$ of the particles evolve according to Newton's equation of motion:

$$\frac{\partial}{\partial t} \boldsymbol{r}_i = \boldsymbol{v}_i(t), \tag{4}$$

$$m_i \frac{\partial}{\partial t} \boldsymbol{v}_i = \boldsymbol{F}_i = -\sum_{j \neq i} \nabla U(r_{ij}), \tag{5}$$

where m_i is the mass and $\boldsymbol{F}_i$ is the force on particle i. The interaction potential $U(r_{ij})$ models the physics of the system under consideration. Here, we consider liquid argon as a Lennard–Jones fluid interacting with a carbon nanotube. We implement an interaction potential as

$$U(r_{ij}) = U_{12-6}^{AB}(r_{ij}) + U_{\mathrm{m}}(r_{\mathrm{w}}; \rho, T) \tag{6}$$

with a two body Lennard–Jones interactions between particles of type A and B at a distance of r_{ij}

$$U_{12-6}^{AB}(r_{ij}) = 4\epsilon_{AB} \left[\left(\frac{\sigma_{AB}}{r_{ij}} \right)^{12} - \left(\frac{\sigma_{AB}}{r_{ij}} \right)^{6} \right], \tag{7}$$

with energy and length parameters ϵ_{AB} and σ_{AB}.

The Lennard–Jones interaction parameters for the argon–argon and argon–CNT interactions are $\epsilon_{\mathrm{ArAr}} = 0.996$ kJ mol^{-1}, $\sigma_{\mathrm{ArAr}} = 0.340$ nm, $\epsilon_{\mathrm{ArC}} = 0.570$ kJ mol^{-1}, and $\sigma_{\mathrm{ArC}} = 0.340$ nm, respectively. The carbon nanotube is modeled as a rigid structure [17]. The term $U_{\mathrm{m}}(r_{\mathrm{w}}; \rho, T)$ accounts for the interaction of the atomistic region with the surrounding medium and depends on the distance to the outer boundary of the atomistic domain r_{w}, the local density ρ, and the local temperature T of the fluid and is further described in Section 3.1. All interaction potentials are truncated for distances beyond a cutoff radius r_c of 1.0 nm. The equations of motion (4) and (5) are integrated using the leap-frog scheme [16] with a time step δt of 5 fs. When appropriate, we report quantities in terms of reduced units, where ϵ_{ArAr}, σ_{ArAr}, and m_{Ar} are the energy, length, and mass units used for the non-dimensionalization. Thus, the reduced temperature, density, and pressure are $T^+ = k_{\mathrm{B}} T / \epsilon_{\mathrm{ArAr}}$, $\rho^+ = \rho \sigma_{\mathrm{ArAr}}^3$, and $P^+ = P \sigma_{\mathrm{ArAr}}^3 / \epsilon_{ArAr}$, respectively.

3.1. Effective boundary potential and force for a monatomic fluid

MD simulations are often being employed for homogeneous systems. In this case, periodic boundary conditions are useful in minimizing boundary effects. However, in the context of the hybrid simulations considered herein, it is necessary to impose arbitrary non-periodic boundary conditions (NPBC). These NPBC can be imposed through a boundary model that is required to:

(A1) exert the correct mean pressure on the MD system and
(A2) minimize any kind of local disturbance (e.g., in the density or temperature fields).

We consider the first criteria (A1) as mandatory, while the second (A2) is motivated by the attempt to minimize the extent of the MD domain. Note that a boundary model that explicitly accounts only for the first first criterion (A1) may still work as long as the boundary is sufficiently far away from the zone of interest. To satisfy (A1), the effective force F_m on the MD system has to correspond to the mean virial part of the system pressure P_U, i.e.,

$$P = P_K + P_U = k_B T \rho_n + \rho_n \int_0^{r_c} F_m(r)\,dr, \tag{8}$$

where P_K denotes the ideal part of the pressure and k_B is the Boltzmann constant.

A number of boundary force models have been employed in related works on hybrid schemes for the simulation of dense fluids [7–10,4,12]. We have implemented these models and have analyzed their advantages and drawbacks. Based on this analysis we propose a novel boundary model that includes an effective boundary potential and a specular wall allowing for a non-zero mean fluid velocity. All force expressions are given along the outward normal n and the subscript w is omitted for clarity, i.e., r denotes the distance to the wall.

A constant repulsive force has been proposed in O'Connell et al. [7]

$$F_m = -\alpha P \rho_n^{-2/3}, \tag{9}$$

where P is the pressure of the system, and α an adjustable parameter. Flekkøy et al. [8] and Delgado-Buscalioni and Coveney [9] used a weighting function $w(r)$ that distributes (cell-wise) the mean pressure force $F = PA$ on the particles as

$$F_m(r_i) = -\frac{w(r_i)}{\sum_j w(r_j)} PA. \tag{10}$$

In Delgado-Buscalioni and Coveney [9], a uniform weighting function $w_u(r) = 1$ has been used while Flekkøy et al. [8] have employed a diverging weighting function $w_d(r) = 1/r - 2/r_c + r/r_c^2$. Finally, Nie et al. [12] have applied a diverging force at the boundary of the form

$$F_m(r) = -\beta P \sigma \frac{r_c - r}{1 - (r_c - r)/r_c}, \tag{11}$$

where β is an adjustable parameter. Clearly, the models based on Eq. (10) satisfy (A1) by construction and so does the expression (9) when $\alpha = 1/(\rho_n^{1/3} r_c)$. On the other hand, the pressure exerted on the system by the force (11) is infinitely large and this model in this form is not recommended. To allow a comparison to the other models, we include Eq. (11) in the following shifted form:

$$F_m(r) = \begin{cases} -\beta P \sigma \frac{r_c - r_b - r}{1 - (r_c - r_b - r)/r_c} & \text{for } r < r_c - r_b, \\ 0, & \text{otherwise,} \end{cases} \tag{12}$$

where the shift r_b is computed from the expression $\rho_n \int_{r_b}^{r_c} F_m(r)\,dr = P$. In other hybrid simulations, Hadjiconstantinou and co-workers [10,4] considered examples where periodic boundary conditions were applicable and where therefore no effective boundary potential was needed.

We propose to apply an effective boundary force that addresses (A2) by accounting for the local structure of the fluid, which for a monatomic fluid is described by the radial distribution function $g(r)$. In this model, we integrate the force components normal to the wall and the potential energy contributions weighted by $g(r)$ over the part of the cutoff sphere that lies outside of the atomistic domain, cf. Fig. 2.
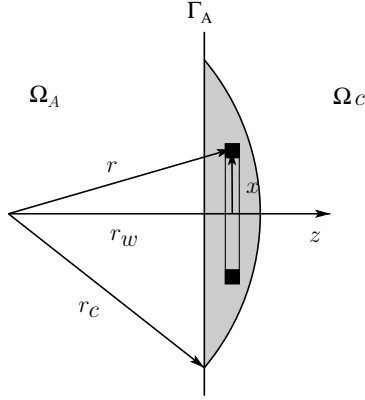
Fig. 2. Integration domains for the effective boundary force and potential (13) and (14). The force and potential contributions along z are integrated over the shaded area using polar coordinates. The number of atoms in the infinitesimal ring element is $2\pi\rho_n g(r)x\,dx\,dz$, where ρ_n is the average number density and $g(r)$ the radial distribution function.

The integration is performed in polar coordinates, where z is normal to the boundary and x denotes the radial direction as:

$$F_{\mathrm{m}}(r_{\mathrm{w}}) = -2\pi\rho_n \int_{z=r_{\mathrm{w}}}^{r_{\mathrm{c}}} \int_{x=0}^{\sqrt{r_{\mathrm{c}}^2-z^2}} g(r)\frac{\partial U_{12-6}(r)}{\partial r}\frac{z}{r}x\,dx\,dz, \tag{13}$$

$$U_{\mathrm{m}}(r_{\mathrm{w}}) = 2\pi\rho_n \int_{z=r_{\mathrm{w}}}^{r_{\mathrm{c}}} \int_{x=0}^{\sqrt{r_{\mathrm{c}}^2-z^2}} g(r)U_{12-6}(r)x\,dx\,dz, \tag{14}$$

where r_{c} is the cutoff radius, ρ_n is the average number density, $r = \sqrt{x^2 + z^2}$, and r_{w} the distance to Γ_{A}. The $F_{\mathrm{m}}(r)$ and $U_{\mathrm{m}}(r)$ for a Lennard–Jones fluid can be obtained by either using a readily available parametrization of $g(r)$ as proposed by Matteoli and Ali Mansoori [18] and performing the integration in (13) and (14) or by evaluating the integrals (13) and (14) explicitly in a separate simulation. In this work we have adopted both approaches. In the Appendix A of the paper, we describe the measurement of $F_{\mathrm{m}}(r)$ and $U_{\mathrm{m}}(r)$ in an MD simulation and report low order polynomial fits describing these terms.

In Fig. 3, the different effective boundary force terms are displayed. An important feature of the force F_{m} (13) is the existence of a pronounced attractive component experienced by the particles near the boundary. All previous models (see Eqs. (9)–(12)) included only repulsive force components. This leads to the well known layering of particles close to a wall as demonstrated in Section 5. The boundary force based on the parametrization of $g(r)$ from [18] is in excellent agreement with Eq. (A.1) for $r_{\mathrm{w}} > \sigma$ but closer to the boundary, there is a significant difference. This difference can be explained by the deviation of the parametrized $g(r)$ to the one observed in the simulation at the same state point (not shown). In the subsequent simulations, we use the measured boundary force and potential described in Appendix A.

3.2. Particle reflections and insertions

A mechanism is necessary in the boundary region Γ_{A} in order to handle particles leaving the domain when imposing NPBC. It is important to realize that particles may leave the atomistic domain Ω_{A} even though a boundary force model is applied in order to account for the interaction of the atomistic region with the surrounding medium. Thus, without further constraints, particles will constantly leave the atom-
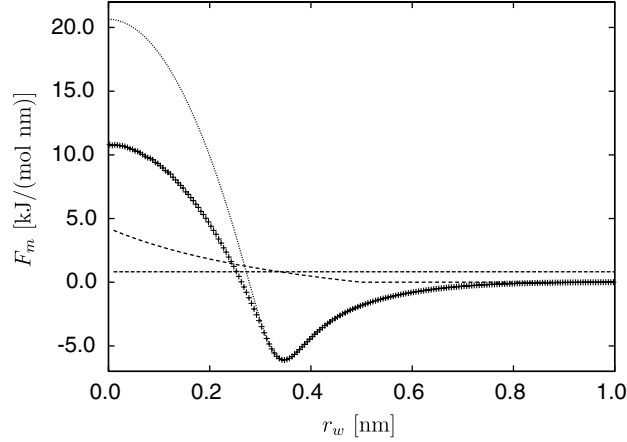
Fig. 3. Effective boundary force F_m on a Lennard–Jones particle located at a distance r_w from the boundary of an atomistic system of density $\rho = 1.0$ g cm^{-3} and at temperature $T = 215$ K. Displayed are the constant force from Eq. (9) with $\alpha = 0.404$ (——), the shifted diverging force (12) ($\beta = 1$) (– –), Eq. (13) evaluated with $g(r)$ from [18] ($\cdots$), and the force as measured in a simulation (+).

istic region across the outer boundary Γ_A. Since our model simulates a steady, incompressible flow, the total number of particles in the atomistic system needs to be overall constant. In order to preserve the number of particles in the system, the outer boundary Γ_A is modeled as an impermeable wall. This specifies the density in Ω_A to a constant value and ensures mass conservation. Particles that strike the wall are specularly reflected, i.e., their velocity components normal to the wall are reversed while the other components are not altered by the impact. A specular wall acts as a plane of symmetry and the rebounded particles can be looked at as if they had come from an imaginary particle reservoir on the other side of the wall [19]. The boundary model equation (13) takes the mean effect of this imaginary particle reservoir into account and prevents density perturbations close to the wall. The symmetric extension of the system by the specular wall is thus justified and the ideal part of the pressure P_K equals $k_B T \rho_n$ at the boundary. We note that the *instantaneous* momentum of the atomistic system is altered by every single particle reflection, however, the average momentum remains constant.

In case a mean flow is imposed across Γ_A, the specular walls move with the local cell velocity, cf. Fig. 4. In other words, in every time step, the collisions of the particles with the specular walls are evaluated in a frame of reference that moves with the local fluid velocity. At the end of the time step, the walls are reset on Γ_A leaving some particles outside of the computational domain. The average number of such particles amounts to the required value of $\rho_N \delta t A \mathbf{u} \cdot \mathbf{n}$ since ρ_N is uniform and $\mathbf{u}$ prescribed by the body force described in Section 3.3. These particles are collected and reintroduced into the system as described later. To find the particles that strike a moving wall in direction x during time step n, we compute the collision time as $t' = (x^n - \tilde{x}_W)/(u_x - \tilde{v}_x^{n+1/2})$, where $\tilde{x}_w$ and u_x are the initial wall position and the wall speed, and $\tilde{v}_x^{n+1/2}$ is the particle velocity after the regular leap-frog position update but before a possible reflection. A particle crosses the system boundary Γ_A if $0 \leqslant t' \leqslant \delta t$ and the new velocity and position in the x-direction are computed as

$$v_x^{n+1/2} = -(\tilde{v}_x^{n+1/2} - u_x) + u_x \tag{15}$$

and

$$x^{n+1} = x^n + t'\tilde{v}_x^{n+1/2} + (\delta t - t')v_x^{n+1/2}, \tag{16}$$

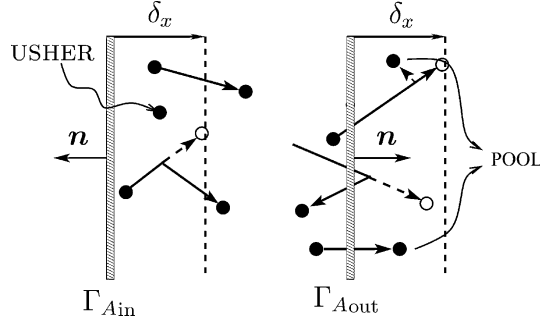while the y- and z-components remain unchanged.

Fig. 4. Schematic representation of the boundary model for the atomistic system at an inlet face $\Gamma_{A_{in}}$ and an outlet face $\Gamma_{A_{out}}$, cf. also Fig. 1. The specular walls move in every time step δt with the local fluid velocity $\boldsymbol{u}$ along the face normal $\boldsymbol{n}$, i.e., their total displacement along x is $\delta_x = u_x n_x \mathrm{d}t$. The dashed arrows denote the original particle trajectories before reflection with the wall. Particles that leave the system are reintroduced through an inlet face, cf. text.

For the particles that have to be reintroduced, a cell face of Γ_A is randomly chosen among those that have a net inflow ($\boldsymbol{n} \cdot \boldsymbol{u} < 0$) and with a probability proportional to the local inflow ($|\boldsymbol{n} \cdot \boldsymbol{u}|$). This distribution scheme is simple and proved to be more efficient than an alternative scheme that we tested which is based on the instantaneous density in the inflow cells. This latter scheme was found to be inefficient as the magnitude of the local density fluctuations is large compared to the number of particles that have to be introduced on average.

Once a target cell face is selected, the USHER algorithm [20] is used to find a particle location with a potential energy corresponding to the mean potential energy e_0 in the system. The USHER algorithm performs a steepest descent method in the energy landscape and applies appropriate heuristics to avoid computationally expensive line searches. In [9], the starting positions for the steepest descent are chosen randomly in the entire cell. Here, we choose the starting positions according to the probability that a particle would actually enter at a distance r_w from the given cell face, i.e.,

$$P(r_w) = c\rho_N \int_{-\infty}^{0} f_T((r_w - x)/\delta t)\, \mathrm{d}x = \frac{\delta t \rho_N}{2}\left(1 + \mathrm{erf}\left[\sqrt{\frac{m}{2k_B T}}\left(u_n - \frac{r_w}{\delta t}\right)\right]\right), \tag{17}$$

where f_T is a Maxwell distribution defined in Eq. (19), c a normalization constant, and u_n is the imposed mean velocity. Additionally, we limit the search space to be of thickness L_s given by $\int_0^{L_s} P(x)\, \mathrm{d}x = 0.99$. When the steepest descent path leads outside of the search space then the search is restarted with a new random initial position.

The wall normal component v_n of the velocity of the introduced atom is sampled from a Rayleigh distribution [21]

$$f_N(v_n) = \frac{m}{k_B T}|v_n|\exp\left(-\frac{m(v_n - u_n)^2}{2k_B T}\right), \tag{18}$$

and the tangential components v_t are sampled from a Maxwell distribution

$$f_T(v_t) = \sqrt{\frac{m}{2\pi k_B T}}\exp\left(-\frac{m(v_t - u_t)^2}{2k_B T}\right). \tag{19}$$

By construction, the new particle has a potential energy of e_0, which implies that the total potential energy added to the system per particle insertion is $2e_0$, and thus the new mean energy of the system becomes $e_0' = (N+2)/(N+1)e_0$, where N denotes the total number of particles.

3.3. Imposition of mean velocity and thermostatting mechanism

In order to enforce the continuum velocity field $\boldsymbol{u}_k$ on the cells k in Γ_{A}, a body force $\boldsymbol{b}_k$ is applied in every time step to adjust the instantaneous center-of-mass velocity [3]

$$\bar{\boldsymbol{v}}_k = 1/N_k \sum_{i \in k} \boldsymbol{v}_i. \tag{20}$$

The body force is adjusted so as to yield in every time step the center of mass velocity $\boldsymbol{u}_k$ as prescribed by the continuum ($\bar{\boldsymbol{v}}_k^{n+1/2} = \boldsymbol{u}_k$). The value of the body force $\boldsymbol{b}_k^n$ in cell k at time $n\delta t$ is found from the velocity update formula of the leap-frog scheme [16]

$$\bar{\boldsymbol{v}}_k^{n+1/2} = \bar{\boldsymbol{v}}_k^{n-1/2} + \frac{\delta t}{N_k m_{\mathrm{Ar}}} \left(\boldsymbol{f}_k^n + \boldsymbol{b}_k^n \right), \tag{21}$$

where $\boldsymbol{f}_k^n$ is the total force acting on the center of mass of cell k and δt is the time step. Thus, the required body force is

$$\boldsymbol{b}_k^n = \frac{N_k m_{\mathrm{Ar}}}{\delta t} \left(\boldsymbol{u}_k - \bar{\boldsymbol{v}}_k^{n-1/2} \right) - \boldsymbol{f}_k^n. \tag{22}$$

We note that this driving mechanism corresponds to the constraint dynamics algorithm introduced by O'Connell et al. [7]. The fluid is kept at the target temperature T by a cell-wise Berendsen thermostat [22] in the z-direction. All flows considered in the present work are homogeneous in the z-direction, the thermostat does therefore not influence the streaming velocities.

4. The macroscopic model

We model the continuum part of the hybrid solution in Ω_{C} as a two-dimensional steady flow of an incompressible, viscous, isothermal fluid which is described by the Navier–Stokes equations in the form [23]

$$\nabla \cdot \boldsymbol{u} = 0, \tag{23}$$

$$(\boldsymbol{u} \cdot \nabla)\boldsymbol{u} = -\frac{1}{\rho}\nabla p + v\Delta\boldsymbol{u}, \tag{24}$$

where $\boldsymbol{u}$ and p are the velocity and pressure fields, ρ is the density, and v is the fluid shear viscosity. The external velocity boundary conditions on $\partial\Omega_{\mathrm{C}}$ can take any admissible form, while Dirichlet boundary conditions are applied on the internal boundary Γ_{C} with values from the atomistic domain $\mathbf{u}|_{\Gamma_{\mathrm{C}}} = \mathbf{u}_{\mathrm{A}}|_{\Gamma_{\mathrm{C}}}$, as described in the following section. We use the commercial flow solver StarCD [24] to solve Eqs. (23) and (24) employing a second-order central difference finite volume discretization and with an equation for the pressure derived using the SIMPLE method [25]. The velocity boundary conditions for the continuum system on the internal boundary Γ_{C} are extracted from the atomistic system as described below.

The only physical parameter that is explicitly needed by the continuum solver is the fluid shear viscosity. In Rowley and Painter [26], a value for the kinematic viscosity of $v = 0.8 \times 10^{-7}$ m^2 s^{-1} is reported for the state point of the Lennard–Jones fluid considered in this work ($\rho^+ = 0.6$, $T^+ = 1.8$, $v^+ = 1.50$). Rowley and Painter estimate the uncertainty in v to be $\pm17.2\%$ and used in their simulations a cutoff of 4σ as compared

to 2.94σ in the present work. The Reynolds number based on the tube diameter D and v is $Re = u_x D / v \approx 1.5$.

4.1. Continuum boundary conditions from the atomistic system

The extraction of average values $\bar{q}$ of a quantity q (e.g., velocity, pressure and density) from the MD trajectories is a straightforward process [16]. However, one has to carefully consider the associated statistical error E_q, which depends on the number of samples M_q used for the average as $E_q = \sigma(\bar{q})/\bar{q} = \sigma(q)/(\sqrt{M_q}\bar{q})$, where $\sigma(q)$ denotes the standard deviation of q. Hadjiconstantinou et al. [13] have given a priori estimates for the number of samples M_u, M_ρ, and M_P needed to measure averages of velocity, density, and pressure, respectively, in a cell of volume V

$$M_u = \frac{k_B T_0}{u_0^2} \frac{1}{\rho_0 V E_u^2}, \quad M_\rho = \frac{\kappa_T k_B T_0}{V E_\rho^2}, \quad M_P = \frac{\gamma k_B T_0}{P_0^2 \kappa_T} \frac{1}{V E_P^2}, \tag{25}$$

where u_0, ρ_0, T_0, and P_0 denote the average velocity, density, temperature, and pressure, k_B is the Boltzmann constant, γ the ratio of specific heats, and κ_T the isothermal compressibility of the fluid. To illustrate the implications of Eq. (25), we consider a numerical example for a hybrid computational domain where the cell volume V over which atomistic quantities are averaged is 1 nm^3. We consider a flow of water at atmospheric conditions ($P_0 = 1$ bar and $T_0 = 293$ K) and with a ratio of specific heats $\gamma = 1$, an isothermal compressibility of $\kappa_T = 48.95 \times 10^{-6}$ bar^{-1}, and a mean velocity $u_0 = 100$ m s^{-1}. Then, to limit the fractional errors E_u, E_ρ, and E_P to 5% the number of required (*statistically independent*) samples amounts to $M_u \approx 10^2$, $M_\rho \approx 1$, and $M_P \approx 10^8$. If the samples are time correlated, the number of samples that are effectively needed increases to $M_q^e = 2\tau_q M_q$, where τ_q is the integrated autocorrelation time [27].

From these estimates we observe that the pressure is particularly expensive to obtain even at this modest accuracy. In flux-based schemes where the pressure tensor is needed one either has to collect a large amount of samples, use a larger cell size (at the cost of having a lower spatial resolution), or apply smoothing schemes such as the thermodynamic field estimator [28]. For these reasons, in this work we favour density-based schemes, where the pressure does not need to be computed or to be imposed directly.

On the other hand, based on the above estimates the computation of cell velocity values is not prohibitive. In order to verify this statement, we determine M_u' in an equilibrium simulation of a Lennard–Jones fluid, compare it to the a priori estimate for M_u of Eq. (25) and finally find M_u^e by taking the time correlation of the samples into account. We consider a fully periodic system with 1619 argon atoms placed in a box of dimensions $5.0 \times 5.0 \times 4.26$ nm and equilibrated at a temperature of $T = 215$ K. From a 10-ns long simulation, we record the time evolution of the average velocity $\boldsymbol{u} = 1/N \sum_k \boldsymbol{v}_k$ in cells of size $0.5 \times 0.5 \times 4.26$ nm, and extract a standard deviation (averaged over the velocity components) of $\sigma_u = 51.2$ m s^{-1}. For $u_0 = 100$ m s^{-1} and a desired fractional error of $E_u = 8\%$, this system requires $M_u' = \sigma(u)^2/u_0^2 E_u^2 \approx 41$ samples. From Eq. (25), we find $M_u \approx 43$ which is in good agreement with the measured M_u'. The integrated autocorrelation time is found to be $\tau_u = 1.25$ ps corresponding to 250 time steps. Thus, in this example the effective number of samples M_u^e needed to achieve the desired accuracy amounts to $M_u^e = 2\tau_u/\delta t M_u = 20,000$.

The velocities on the cell faces Γ_C are obtained from a linear interpolation between the values of the adjacent cells. Additionally, two corrections are applied to the velocity boundary condition in order to prevent (artificial) asymmetries and spurious mass sources or sinks in the continuum solution due to noise in the MD data. First, the velocities on Γ_C are symmetrized with respect to the x-axis. Second, the velocity components prescribed on Γ_C are scaled such that they satisfy the continuity constraint

$$\int_{\Gamma_C} \boldsymbol{u} \cdot \boldsymbol{n} \, ds = 0. \tag{26}$$

In practice, the discrete equivalent of the integral in Eq. (26) is evaluated as the difference $\Delta J = J_{in} - J_{out}$ between the total mass in- and outflux across Γ_C. If $\Delta J \neq 0$, the velocities on influx faces are scaled by a factor $s_{in} = 1 - \Delta J/(2J_{in})$, and those on outflux faces by $s_{out} = 1 + \Delta J/(2J_{out})$, resulting in new total fluxes of $J'_{out} = J_{out} + \Delta J/2$, and $J'_{in} = J_{in} - \Delta J/2$, with $\Delta J' = 0$. In the hybrid example given in Section 5.3, the scale factors were always smaller than $\pm 2\%$.

5. Results

We first demonstrate the validity of the proposed boundary conditions for a purely atomistic system, i.e., without a coupling to a continuum, for the two fundamental cases of an equilibrium and of a uniform parallel flow. The system consists of 1900 argon atoms ($m_{Ar} = 39.948$ a.m.u.) in a cubic box of edge length 5.0 nm equilibrated at a temperature of $T = 215$ K, corresponding to a density of $\rho = 1.008$ g cm^{-3} and a pressure of $P = 653$ bar ($T^+ = 1.8$ and $\rho^+ = 0.6$, $P^+ = 1.55$). [1]

5.1. NPBC for liquid argon at equilibrium

In this section, we consider the effect of applying NPBC to a system of liquid argon in equilibrium. In these simulations, the y- and z-directions are treated periodically, while in the x-direction, the different effective boundary forces as discussed in Section 3.1, are applied. The trajectories of the 2 ns long simulations are stored in time intervals of 0.5 ps and are used to compute density profiles along the x-axis in 250 bins of width 0.2 Å, cf. Fig. 5. The parameter α in the constant force Eq. (9) is chosen as $\alpha = 1/(\rho_n^{1/3} r_c) = 0.404$ and the shift in Eq. (12) as $r_b = 0.500$.

If no boundary force is applied, we observe (Fig. 5) strong density oscillations next to the boundary with a peak at the boundary. The application of any of the discussed effective boundary forces reduces the magnitude of the first peak. However, the first density minimum is amplified when the force from Eq. (9) [7] or those based on (10) [8,9] are applied. The extent of the layering is essentially limited to one cutoff radius but a slightly increased density persists in the central domain whose magnitude depends on the system size. The boundary force (13) proposed herein takes the fluid structure into account and includes an attractive part thus significantly minimizing the density oscillations overall.

5.2. NPBC for a parallel flow of liquid argon

In order to study the capabilities of our scheme to handle dense fluid flows, we use an identical setup as in the previous section, with the addition that a uniform flow is imposed along the x-axis with $u = 100$ m s^{-1}. The computational box is subdivided into $5 \times 5 \times 3$ cells each with volume of 1.67 nm^3. In the USHER algorithm, the mean potential energy e_0 of a particle was a-priori (in a fully periodic simulation) determined to be $e_0 = -3.612$ kJ mol^{-1} and served as a target energy for particle insertions. The relative error in the energy was required to be less than 1% and the step size of the USHER algorithm was limited to $\Delta s_{max} = 0.1(\rho^+)^{-1.5}\epsilon_{ArAr} = 0.073$ nm, as proposed in [20].

We consider three different boundary schemes in the x-direction, while the y- and z-directions are again chosen to be periodic. The first scheme collects all particles that leave the computational domain and uses USHER to reinsert them without any additional measures. The second employs in addition the effective boundary force F_m (13) and uses the potential U_m (14) when inserting particles (F_m and U_m are given in Appendix A). Finally, the third model includes in addition the specular wall as described in Section 3.2.

---

[1] With a standard tail correction applied, cf. [29], one obtains a pressure of $P = 554$ bar ($P^+ = 1.32$).
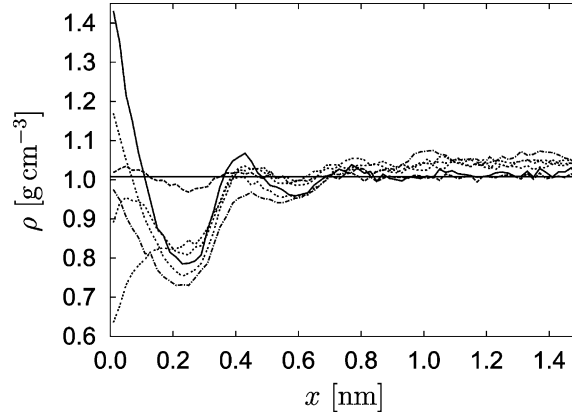
Fig. 5. Density profiles of a Lennard–Jones liquid at $\rho = 1.008$ g cm^{-3} and $T = 215$ K close to specular wall. The following effective boundary forces are applied —: none, - - - -: [7] (Eq. (9)), - - -: [8] (Eq. (10) with w_d), - · -: [9] (Eq. (10) with w_u), - - - - - -: [12] (Eq. (12)), – – –: present work (Eq. (13)), —: reference value of 1.008 g cm^{-3}.

The three schemes have been examined for the same configuration and the density profiles along the flow direction shown in Fig. 6 demonstrate that the third model minimizes density fluctuations significantly. In particular, it effectively removes the mean density gradient observed with the other models.

5.3. Hybrid atomistic–continuum flow around a carbon nanotube

The proposed hybrid atomistic–continuum method is further validated in this section, by considering the flow of liquid argon past a carbon nanotube. We compare the hybrid solution to a reference solution that is obtained by a purely atomistic simulation of the system. In both cases, the computational domain extends over $30 \times 30 \times 4.26$ nm and is centered at the origin. The carbon nanotube is of chirality (16,0) with a radius of $r = 0.626$ nm and is fixed at the origin with its axis parallel to the z-axis.

The external boundary conditions on $\partial\Omega_C$ are periodic in y and of the Dirichlet type at the left $(\partial\Omega_C|_{x = -15.0\,\text{nm}})$ and right $(\partial\Omega_C|_{x = 15.0\,\text{nm}})$ boundaries where a flow velocity of $u_x = 100$ m s^{-1} and $u_y = 0$ m s^{-1} is prescribed. These boundary conditions are straightforward to implement in the purely atomistic
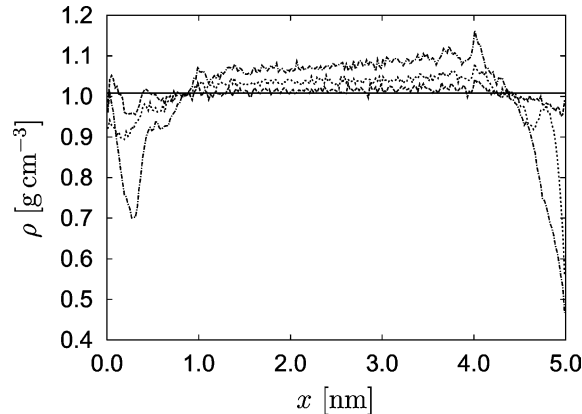

Fig. 6. Density profiles of a Lennard–Jones liquid in non-periodic simulations of a uniform flow with mean velocity 100 m s^{-1}, mean density $\rho = 1.008$ g cm^{-3} and temperature $T = 215$ K. The missing particles outside the computational domain are replaced by nothing (- · -), by an effective force F_m (· · ·), or by F_m and a specular wall (---).

reference simulation, as discussed in Section 3.3. The number of argon atoms for the reference simulation is N_{Ar} = 58268 and results in a density of ρ = 1.008 g cm^{-3} in the far-field of the tube. The simulation is equilibrated for 1 ns and then run for another 4 ns to gather statistics. The statistical error in the averaged cell velocities (1) is estimated to be ± 1.1%, based on the values of $\sigma(u)$ and τ_u given in Section 4.1. During the whole simulation, the z-component of the particle velocities are weakly coupled to a Berendsen thermostat [30] at 215 K with a coupling constant 0.1 ps. The computational domain of the atomistic reference solution and the average velocity in cells of size $0.5 \times 0.5 \times 4.26$ nm are shown in Figs. 7(a) and (c).

For the hybrid simulation, the edge length of the atomistic domain is reduced to L_A = 10 nm and the number of atoms to 6400 corresponding to 1/9 of the original system, cf. Fig. 7(b). The finite volume mesh for the solution of the Navier–Stokes equations in Ω_C consists of cells of size $0.5 \times 0.5 \times 4.26$ nm and overlaps the atomistic domain by four cell widths, i.e., by L_O = 2.0 nm. We arbitrarily choose a uniform velocity with u_x = 100 m s^{-1} and u_y = 0 m s^{-1} as an initial guess for the internal boundary condition on Γ_C. Hence, the solution for the velocity field $\mathbf{u}_C^0$ in the first iteration is a parallel flow.

In Fig. 8, we show the evolution of the u_x velocity component during the iteration along the x- and the y-axis. The noise introduced in the hybrid solution through the atomistic domain prevents the solutions to fully converge. Nevertheless, the profiles are generally in close agreement with the reference solution (solid line) after approximately 20 iterations and do not change more than expected from the noise amplitude. In
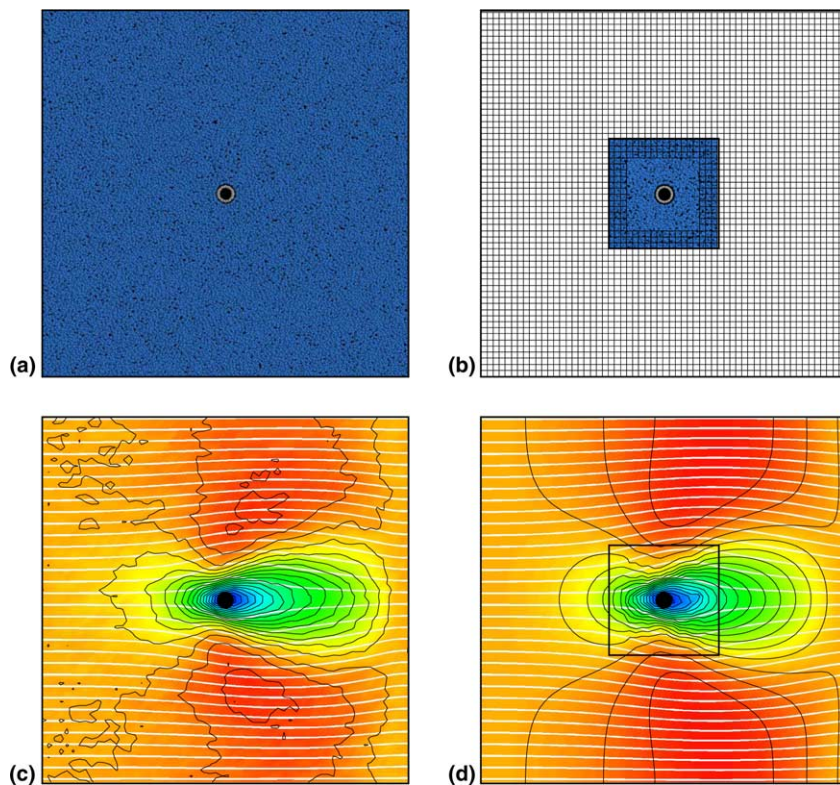

Fig. 7. (a) Computational domain for the reference solution of the flow of argon around a carbon nanotube using a purely atomistic description. (b) Hybrid atomistic/continuum computational domain. Both computational domains have an extent of 30×30 nm. (c) Velocity field for the reference solution averaged over 4 ns. The white lines are streamlines, and the black lines are contours of the speed ($|\mathbf{u}|$). (d) Velocity field of the hybrid solution after 50 iterations. The black square denotes the location of Γ_A. The solution in Ω_A is averaged over 10 iterations.
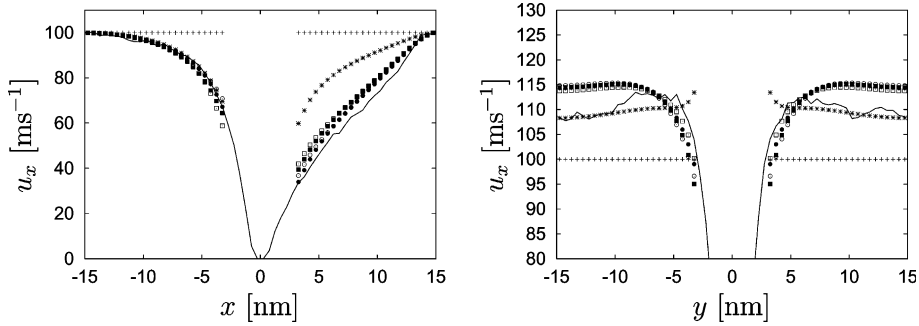
Fig. 8. The u_x velocity component along the x-axis and along the y-axis in the course of a hybrid iterative solution of the flow around a carbon nanotube. The shear viscosity v for the continuum solution is 0.8×10^{-7} m^2 s^{-1}. The solid lines are the velocity components as obtained from a purely atomistic simulation. The symbols denote the kth iteration with $k = 1$ (+), 10 (✳), 20 (□), 30 (■), 40 (○), and 50 (●), respectively.

fact, as proposed in [4], the optimal way to schedule the number of molecular dynamics steps N_k in iteration k should scale as $N_k \propto K^{-k}$, where $0 < K < 1$ is a positive constant. In this way, the statistical error in the boundary condition Γ_C is decreased as the iteration proceeds. Here we did not use such a technique, but the atomistic system is in every iteration run for 40,000 steps whereof the second half is used to determine the next boundary condition on Γ_C. The velocity profile along the x-axis from the inlet towards the stagnation point in front of the carbon nanotube is in good agreement with the reference solution, cf. Fig. 8. We observe differences in the u_x velocity in the wake behind the tube and along the y-axis (Fig. 8). These differences are quantified in the following.

The convergence of the hybrid solution towards the reference solution is depicted in Fig. 9 in terms of the error e^k (1) and the rate of change of the velocity field d^k (3). The error e^k levels off at a value of $\approx 4\%$ after 20 iterations. We have investigated the effect of prolonging the equilibration (40,000 steps) and sampling (60,000 steps) times of the atomistic part of the iteration. The rate of change d^k is reduced, however, the error e^k is not further decreased as can be seen in Fig. 9. We attribute the persistent error to several sources. First of all, the statistical error in the reference solution itself amounts to $\approx \pm 1.1\%$. Second, the spatial resolution of $0.5 \times 0.5 \times 4.26$ nm of the finite volume grid and of the cells in Γ_A may not fully resolve the large velocity gradients present around the tube (Fig. 8). Third, the viscosity v obtained from Rowley and Painter [26] has an uncertainty of $\pm 17.2\%$. The implications of this point are further discussed below. We note that despite the 4% error, there is good agreement between the reference and the hybrid solution, cf. Figs. 7(c) and (d).

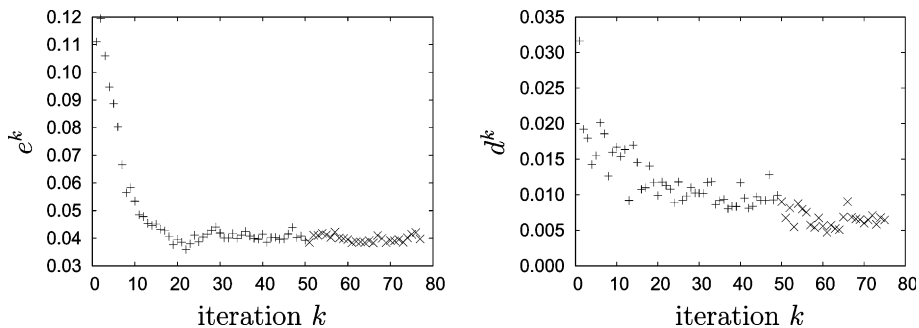Fig. 9. Left: Convergence of the hybrid velocity field towards the MD reference solution in terms of the mean, normalized cell-error Eq. (1). Right: Rate of change (Eq. (3)) of the velocity field in the hybrid solution. In the first fifty iterations (+), the cell velocities are averaged over 2×10^4 MD steps, while in the subsequent 25 iterations (×), the cell velocities are averaged over 6×10^4 time steps.

The mass in the hybrid solution is conserved since the number of particles in Ω_A is constant and since the constraint (26) is enforced. On the other hand, momentum conservation is not explicitly ensured in the Schwarz method. In order to assess the accuracy in momentum conservation of the proposed method we evaluated the drag force on the tube using two different methods. In the first method we computed the drag force on the tube using a surface integral of the stress tensor:

$$D_i^C = \int_S \left[-p\delta_{ij} + v\rho \left(\frac{\partial u_i}{\partial x_j} + \frac{\partial u_j}{\partial x_i} \right) - \rho u_i u_j \right] n_j \, \mathrm{d}A, \tag{27}$$

where the surface S in Ω_C comprises the entire atomistic domain and where index notation has been used. The expression (27) evaluated for the velocity field in the 50th iteration of the hybrid solution yields $D_x^C = 262.5$ kJ mol^{-1} nm^{-1}. The drag force on the tube in the same step of the iteration can also be measured by computing the forces exerted on its atoms. A value of $D_x^A = 261 \pm 6$ kJ mol^{-1} nm^{-1} is obtained from 10^4 samples taken every 0.5 ps of a prolonged simulation, where the velocity boundary conditions of the 50th iteration are constantly applied. We remark that the prolongation of the atomistic simulation decreases the statistical error in measuring D_x^A whose instantaneous values have a large standard deviation of 636.5 kJ mol^{-1} nm^{-1}. This reasonable agreement in the values of $D_x^A = 261 \pm 6$ and $D_x^C = 262.5$ kJ mol^{-1} nm^{-1} represents a measure of momentum conservation for the proposed methodology. As a comparison, we have also computed the Stokes–Oseen drag force $D_x^{SO} = 203$ kJ mol^{-1} nm^{-1} for a flow past an array of two-dimensional circular cylinders (see [3] and the references therein). The value of D_x^{SO} lies within 21% of D_x^A and indicates that the flow pattern of the hybrid solution is similar to the Stokes–Oseen flow. Note that with periodic external boundary conditions in y and uniform Dirichlet boundary conditions in x, we are effectively simulating the flow past an array of CNTs and not past a single CNT. The hybrid atomistic–continuum scheme allows us to implement other external boundary conditions than the ones used in the reference atomistic simulation. As an example, we replaced the Dirichlet boundary conditions at $\partial\Omega_C|_{x\,=\,15.0\,\mathrm{nm}}$ with an outlet boundary condition that extrapolates the velocity and pressure to the boundary on the assumption of zero gradients along the mesh lines, and that adjusts the velocities to satisfy overall continuity [24]. This choice together with the periodicity in y models the flow past a row of CNTs. In Fig. 10, we show that these boundary conditions result in a flow field which is qualitatively
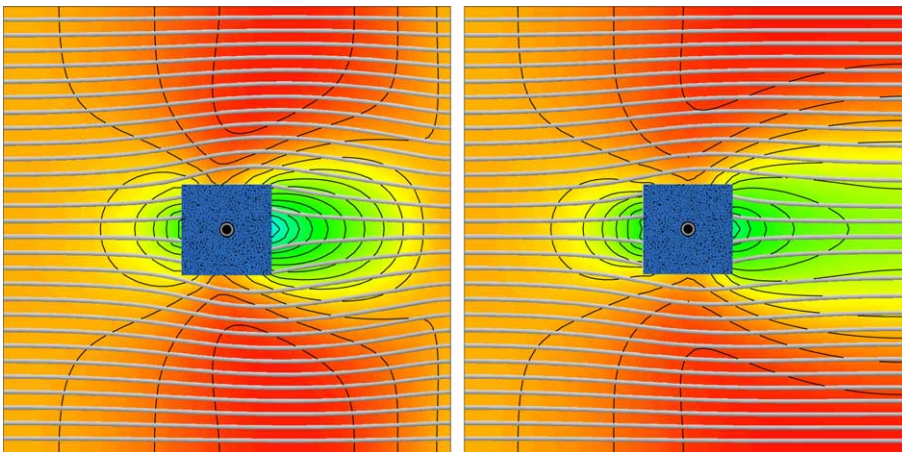
Fig. 10. Comparison of different external boundary conditions for the flow past a carbon nanotube. For both systems, periodic boundary conditions are prescribed in the y-direction and a uniform inlet flow with $u = 100$ m s^{-1} is imposed on the left boundary. The right boundary is either given by a uniform outlet flow velocity of $u = 100$ m s^{-1} (left picture) or by an outlet condition where zero gradients are assumed along the mesh lines (right picture). The white lines are streamlines, and the black lines are contours of the speed ($|\boldsymbol{u}|$).

different to the one obtained with periodic boundary conditions.The freedom allowed in the hybrid scheme to impose arbitrary boundary conditions is an advantage over pure atomistic simulations, since for the latter it is not clear how to implement such outlet conditions.

6. Summary and conclusions

We have presented a novel hybrid scheme that embeds a Molecular Dynamics simulation of a dense Lennard–Jones fluid within a two-dimensional, steady, isothermal, incompressible, continuum fluid mechanics computation. The proposed scheme allows for the first time the atomistic–continuum simulation of dense non-periodic flow fields.

The scheme is formulated in the context of a domain decomposition Schwarz alternating algorithm and requires the extraction and imposition of suitable boundary conditions in the respective subdomains. In order to enforce boundary conditions to the atomistic domain as they are dictated by the continuum, a boundary model is proposed based on an effective boundary potential, specular walls, body forcing terms, and a particle insertion algorithm. The resulting algorithm allows to impose general, non-periodic velocity boundary conditions to the atomistic domain. The boundary model was successfully validated for a hybrid system of a dense fluid in thermodynamic equilibrium and in a uniform parallel flow.

For the coupling of the flow field to the continuum as determined by the atomistic domain, the proposed algorithm requires only velocity boundary conditions. These are substantially easier to extract from the molecular dynamics trajectory than the momentum flux tensor which is needed for flux-based schemes.

We have applied the hybrid scheme to study the flow of liquid argon around a carbon nanotube where the far field of the tube was modeled as a continuum. The resulting flow field was found to be in good agreement with the one obtained for a fully atomistic reference solution. Moreover, we have applied outlet boundary conditions on the external boundary of the continuum and we have shown that this has a significant effect on the flow field. In addition the hybrid scheme allows the imposition of general far-field flow boundary conditions whereas in purely atomistic simulations it is not easy to enforce equivalent outlet boundary conditions. Ongoing work considers the extension of the scheme to allow for more complex fluids such as water. The simulation of water flows would require new efficient molecule insertion algorithm for bonded polyatomic molecules and the formulation of an effective boundary force, in order to properly account for the molecule orientation and the effect of the long range electrostatic interaction.

Appendix A

We here describe the procedure to evaluate the integrals (13) and (14) in an MD simulation. We perform an equilibrium MD simulation in a periodic box at the state point ($\rho^+ = 0.6$ and $T^+ = 1.8$) and sample the mean force felt by a particle k from all particles j with distance $x_{ij} \geqslant r_\mathrm{w}$ and $r_{ij} \leqslant r_\mathrm{c}$. The samples are collected in 200 bins of equal width (0.05 Å) until all have 3×10^6 entries. A piecewise C^1 continuous low order polynomial is fit to the data with the requirements that $F_\mathrm{m}(r_\mathrm{c}) = 0$, $F'_\mathrm{m}(r_\mathrm{c}) = 0$, and $F'_\mathrm{m}(0) = 0$

$$F_{\mathrm{m}}(r_{\mathrm{w}}) = \begin{cases} F_{\mathrm{m}_1}(r_{\mathrm{w}}) & \text{for } 0.0000 < r_{\mathrm{w}} < 0.2975 \text{ nm}, \\ F_{\mathrm{m}_2}(r_{\mathrm{w}}) & \text{for } 0.2975 < r_{\mathrm{w}} < 0.3475 \text{ nm}, \\ F_{\mathrm{m}_3}(r_{\mathrm{w}}) & \text{for } 0.3475 < r_{\mathrm{w}} < 0.3975 \text{ nm}, \\ F_{\mathrm{m}_4}(r_{\mathrm{w}}) & \text{for } 0.3975 < r_{\mathrm{w}} < 1.0000 \text{ nm}, \end{cases} \quad (\text{A.1})$$

where (in units of kJ mol^{-1} nm^{-1})

$$F_{\mathrm{m}_1}(r_{\mathrm{w}}) = 10.8007 + 0.860717 r_{\mathrm{w}} - 172.468 r_{\mathrm{w}}^2 + 86.9134 r_{\mathrm{w}}^3 - 140.214 r_{\mathrm{w}}^4,$$
$$F_{\mathrm{m}_2}(r_{\mathrm{w}}) = -3621.30 + 44657.4 r_{\mathrm{w}} - 204844.0 r_{\mathrm{w}}^2 + 414123.0 r_{\mathrm{w}}^3 - 311674.0 r_{\mathrm{w}}^4,$$
$$F_{\mathrm{m}_3}(r_{\mathrm{w}}) = 4331.63 - 45188.5 r_{\mathrm{w}} + 176236.0 r_{\mathrm{w}}^2 - 305157.0 r_{\mathrm{w}}^3 + 198111.0 r_{\mathrm{w}}^4,$$
$$F_{\mathrm{m}_4}(r_{\mathrm{w}}) = -94.4796 + 576.282 r_{\mathrm{w}} - 1436.11 r_{\mathrm{w}}^2 + 1804.53 r_{\mathrm{w}}^3 - 1133.47 r_{\mathrm{w}}^4 + 283.244 r_{\mathrm{w}}^5.$$

Note that the relation $F_{\mathrm{m}}(r_{\mathrm{w}}) = -\partial U_{\mathrm{m}}(r_{\mathrm{w}})/\partial r_{\mathrm{w}}$ does not hold. It is therefore necessary to measure $U_{\mathrm{m}}(r_{\mathrm{w}})$ separately, and we obtain the following fit to the data

$$U_{\mathrm{m}}(r_{\mathrm{w}}) = \begin{cases} U_{\mathrm{m}_1}(r_{\mathrm{w}}) & \text{for } 0.0000 < r_{\mathrm{w}} < 0.2975 \text{ nm}, \\ U_{\mathrm{m}_2}(r_{\mathrm{w}}) & \text{for } 0.2975 < r_{\mathrm{w}} < 0.4975 \text{ nm}, \\ U_{\mathrm{m}_3}(r_{\mathrm{w}}) & \text{for } 0.4975 < r_{\mathrm{w}} < 1.0000 \text{ nm}, \end{cases} \quad (\text{A.2})$$

where

$$U_{\mathrm{m}_1}(r_{\mathrm{w}}) = -3.61052 + 7.63385 r_{\mathrm{w}},$$
$$U_{\mathrm{m}_2}(r_{\mathrm{w}}) = 9.75231 - 137.022 r_{\mathrm{w}} + 571.665 r_{\mathrm{w}}^2 - 970.06 r_{\mathrm{w}}^3 + 589.472 r_{\mathrm{w}}^4,$$
$$U_{\mathrm{m}_3}(r_{\mathrm{w}}) = -3.45593 + 13.5024 r_{\mathrm{w}} - 20.1245 r_{\mathrm{w}}^2 + 13.5656 r_{\mathrm{w}}^3 - 3.48753 r_{\mathrm{w}}^4.$$

The consistency of the boundary force (A.1) with the pressure in the simulation is excellent, i.e., P_U, evaluated at the wall according to Eq. (8) yields $P_U = 207$ bar ($P_U^+ = 0.49$), which lies within 1% of the virial part of the bulk pressure measured in a separate periodic control system at the same state point.

References

[1] P. Koumoutsakos, U. Zimmerli, T. Werder, J.H. Walther, Nanoscale fluid mechanics. The handbook of nanotechnology and nanometer structures, Theory Model. Simulat. (2004) 319–393.

[2] T. Werder, J.H. Walther, R.L. Jaffe, T. Halicioglu, P. Koumoutsakos, On the water–graphite interaction for use in MD simulations of graphite and carbon nanotubes, J. Phys. Chem. B 107 (2003) 1345–1352.

[3] J.H. Walther, T. Werder, R.L. Jaffe, P. Koumoutsakos, Hydrodynamic properties of carbon nanotubes, Phys. Rev. E 69 (2004) 062201.

[4] N.G. Hadjiconstantinou, Hybrid atomistic–continuum formulations and the moving contact-line problem, J. Comput. Phys. 154 (1999) 245–265.

[5] A.L. Garcia, J.B. Bell, W.Y. Crutchfield, B.J. Alder, Adaptive mesh and algorithm refinement using direct simulation Monte Carlo, J. Comput. Phys. 154 (1999) 134–155.

[6] Q.H. Sun, I.D. Boyd, G.V. Candler, A hybrid continuum/particle approach for modeling subsonic, are field gas flow, J. Comput. Phys. 194 (1) (2004) 256–277.

[7] S.T. O'Connell, P.A. Thompson, Molecular dynamics-continuum hybrid computations: A tool for studying complex fluid flow, Phys. Rev. E 52 (6) (1995) R5792–R5795.

[8] E.G. Flekkøy, G. Wagner, J. Feder, Hybrid model for combined particle and continuum dynamics, Europhys. Lett. 52 (3) (2000) 271–276.

[9] R. Delgado-Buscalioni, P.V. Coveney, Continuum-particle hybrid coupling for mass, momentum, and energy transfers in unsteady flow, Phys. Rev. E 67 (2003) 046704-1–0467040-13.

[10] N.G. Hadjiconstantinou, A.T. Patera, Heterogeneous atomistic–continuum representations for dense fluid systems, Int. J. Mod. Phy. C 8 (4) (1997) 967–976.

[11] G. Wagner, E. Flekkøy, J. Feder, T. Jossang, Coupling molecular dynamics and continuum dynamics, Comp. Phys. Commun. 147 (2002) 670–673.

[12] X.B. Nie, S.Y. Chen, W.N. E, M.O. Robbins, A continuum and molecular dynamics hybrid method for micro- and nano-fluid flow, J. Fluid Mech. 500 (2004) 55–64.

[13] N.G. Hadjiconstantinou, A.L. Garcia, M.Z. Bazant, G. He, Statistical error in particle simluations of hydrodynamic phenomena, J. Comput. Phys. 187 (2003) 274–297.

[14] B.F. Smith, P.E. Bjorstad, W.D. Gropp, Domain Decomposition. Parallel Multilevel Methods for Elliptic Partial Cambridge University Press, Cambridge University Press, 1996.

[15] M. Tysanner, A.L. Garcia, Measurement bias of fluid velocity in molecular simulations, J. Comput. Phys. 196 (2004) 173–183.

[16] M.P. Allen, D.J. Tildesley, Computer Simulation of Liquids, Clarendon Press Oxford, Oxford, 1987.

[17] J.H. Walther, R. Jaffe, T. Halicioglu, P. Koumoutsakos, Carbon nanotubes in water: Structural characteristics and energetics, J. Phys. Chem. B 105 (2001) 9980–9987.

[18] E. Matteoli, G. Ali Mansoori, A simple expression for radial distribution functions of pure fluids and mixtures, J. Chem. Phys. 103 (11) (1995) 4672–4677.

[19] J.C. Maxwell, On stress in rarefied gases arising from inequalities of temperature, Phil. Trans. Roy. Soc. London 170 (1879) 231–256.

[20] R. Delgado-Buscalioni, P.V. Coveney, USHER: An algorithm for particle insertion in dense fluids, J. Chem. Phys. 119 (2) (2003) 978–987.

[21] G.A. Bird, Molecular Gas Dynamics and the Direct Simulation of Gas Flows, Clarendon Press Oxford, Oxford, 1994.

[22] H.J.C. Berendsen, J.P.M. Postma, W.F. van Gunsteren, A. DiNola, J.R. Haak, Molecular dynamics with coupling to an external bath, J. Chem. Phys. 81 (8) (1984) 3684–3684.

[23] L.D. Landau, E.M. Lifshitz, Fluid Mechanics, second ed., vol. 6, Pergamon Press, 1987.

[24] STAR-CD version 3.1a. manual (1999).

[25] S.V. Patankar, D.B. Spalding, Calculation procedure for heat, mass and momentum-transfer in 3-dimensional parabolic flows, Int. J. Heat Mass Transfer 15 (10) (1972) 1787–1806.

[26] R.L. Rowley, M.M. Painter, Diffusion and viscosity equations of state for a Lennard–Jones fluid obtained from molecular dynamics simulations, IJT 18 (5) (1997) 1109–1121.

[27] W. Janke, Statistical analysis of simulations: Data correlations and error estimation, in: G. Johannes, D. Marx, A. Muramatsu (Eds.), Quantum Simulations of Complex Many-Body Systems: From Theory to Algorithms, John von Neumann Institute for Computing (NIC), 2002, pp. 423–445.

[28] J. Li, D. Liao, S. Yip, Coupling continuum to molecular-dynamics simulation: Reflecting particle method and the field estimator, Phys. Rev. E 57 (6) (1998) 7259–7267.

[29] J.K. Johnson, J.A. Zollweg, K.E. Gubbins, The Lennard–Jones equation of state revisited, MP 78 (3) (1993) 591–618.

[30] H.J.C. Berendsen, J.P.M. Postma, W.F. van Gunsteren, J. Hermans, Interaction models for water in relation to protein hydration, in: B. Pullman (Ed.), Intermolecular forces. Proceedings of the Fourteenth Jerusalem Symposium on Quantum Chemistry and Biochemistry, Reidel, Dordrecht, 1981, pp. 331–342.